

Cryo-EM structure of islet amyloid polypeptide fibrils reveals similarities with amyloid- β fibrils

Citation for published version (APA):

Roeder, C., Kupreichyk, T., Gremer, L., Schaefer, L. U., Pothula, K. R., Ravelli, R. B. G., Willbold, D., Hoyer, W., & Schroeder, G. F. (2020). Cryo-EM structure of islet amyloid polypeptide fibrils reveals similarities with amyloid- β fibrils. *Nature Structural and Molecular Biology*, 27(7), 660-667.
<https://doi.org/10.1038/s41594-020-0442-4>

Document status and date:

Published: 01/07/2020

DOI:

[10.1038/s41594-020-0442-4](https://doi.org/10.1038/s41594-020-0442-4)

Document Version:

Publisher's PDF, also known as Version of record

Document license:

Taverne

Please check the document version of this publication:

- A submitted manuscript is the version of the article upon submission and before peer-review. There can be important differences between the submitted version and the official published version of record. People interested in the research are advised to contact the author for the final version of the publication, or visit the DOI to the publisher's website.
- The final author version and the galley proof are versions of the publication after peer review.
- The final published version features the final layout of the paper including the volume, issue and page numbers.

[Link to publication](#)

General rights

Copyright and moral rights for the publications made accessible in the public portal are retained by the authors and/or other copyright owners and it is a condition of accessing publications that users recognise and abide by the legal requirements associated with these rights.

- Users may download and print one copy of any publication from the public portal for the purpose of private study or research.
- You may not further distribute the material or use it for any profit-making activity or commercial gain.
- You may freely distribute the URL identifying the publication in the public portal.

If the publication is distributed under the terms of Article 25fa of the Dutch Copyright Act, indicated by the "Taverne" license above, please follow below link for the End User Agreement:

www.umlib.nl/taverne-license

Take down policy

If you believe that this document breaches copyright please contact us at:

repository@maastrichtuniversity.nl

providing details and we will investigate your claim.



Cryo-EM structure of islet amyloid polypeptide fibrils reveals similarities with amyloid- β fibrils

Christine Röder^{1,2,3,6}, Tatsiana Kupreichyk^{1,2,3,6}, Lothar Gremer^{1,2,3}, Luisa U. Schäfer^{1,2}, Karunakar R. Pothula^{1,2}, Raimond B. G. Ravelli^{1,2}, Dieter Willbold^{1,2,3}, Wolfgang Hoyer^{1,2,3} and Gunnar F. Schröder^{1,2,5}

Amyloid deposits consisting of fibrillar islet amyloid polypeptide (IAPP) in pancreatic islets are associated with beta-cell loss and have been implicated in type 2 diabetes (T2D). Here, we applied cryo-EM to reconstruct densities of three dominant IAPP fibril polymorphs, formed *in vitro* from synthetic human IAPP. An atomic model of the main polymorph, built from a density map of 4.2-Å resolution, reveals two S-shaped, intertwined protofilaments. The segment 21-NNFGAIL-27, essential for IAPP amyloidogenicity, forms the protofilament interface together with Tyr37 and the amidated C terminus. The S-fold resembles polymorphs of Alzheimer's disease (AD)-associated amyloid- β (A β) fibrils, which might account for the epidemiological link between T2D and AD and reports on IAPP-A β cross-seeding *in vivo*. The results structurally link the early-onset T2D IAPP genetic polymorphism (encoding Ser20Gly) with the AD Arctic mutation (Glu22Gly) of A β and support the design of inhibitors and imaging probes for IAPP fibrils.

Pancreatic islet amyloid deposits are a hallmark of T2D. Islet amyloid, first reported almost 120 years ago as islet hyaline¹, is found in >90% of individuals with T2D^{2,3}. The main constituents of islet amyloid are fibrillar aggregates of the 37-residue polypeptide hormone IAPP, also called amylin. IAPP is detected in many organs, including the brain, but is mainly localized in the beta-cells of pancreatic islets, where it is co-synthesized and co-secreted with insulin^{3,4}. IAPP is involved in glucose homeostasis and metabolism, with putative functions as a regulator of insulin and glucagon secretion, satiety and gastric emptying^{3,5}. Formation of toxic IAPP amyloid aggregates has been associated with dysfunction and death of beta-cells, placing T2D in the group of protein misfolding disorders^{2,3,5–8}. However, the nature of the toxic IAPP species and the mechanisms of beta-cell death are not well determined⁹. Potential toxic effects of IAPP amyloid include induction of apoptosis¹⁰, chronic inflammation¹¹, defects in autophagy^{12,13}, endoplasmic reticulum stress^{14,15} and membrane disruption¹⁶. Apart from its association with T2D, IAPP amyloid might also play a role in type 1 diabetes^{10,17}.

IAPP interacts with amyloidogenic proteins that trigger other protein misfolding disorders^{18–20}. Of particular interest is its relation to the A β peptide, the main component of senile plaques found in the brain tissue of patients with AD. IAPP and A β are infamous not only for their strong aggregation propensity and the insolubility of their aggregates³, but also for their primary sequence similarity²¹. IAPP and A β colocalize in A β deposits in the brain tissue of patients with AD¹⁹. Mutual cross-seeding of IAPP and A β aggregation observed in transgenic mice further supports a role of the IAPP–A β interaction in pathogenesis^{19,20}.

Structural information on IAPP amyloid is fundamental for improving understanding of the mechanism of amyloid formation,

for defining toxic IAPP species and for elucidating IAPP–A β cross-seeding^{5,7}. Furthermore, high-resolution IAPP fibril structures can inform the design of fibril growth inhibitors and support the development of soluble, nontoxic IAPP analogs for co-formulation with insulin and leptin for treatment of type 1 diabetes and obesity, respectively⁵. Current structural models of IAPP fibrils at physiological pH based on, for example, solid-state NMR (ssNMR) of full-length IAPP and X-ray crystallography of IAPP fragments consistently place the majority of the 37 amino acid residues into the fibril core, while the N terminus is located at the periphery^{22–27}. Conversely, the available models also exhibit substantial differences, which could be either a consequence of the limited, distinct restraints obtained by the different techniques applied or a reflection of IAPP fibril polymorphism^{5,28}. Here, we have applied cryo-EM to determine the structure of IAPP amyloid fibrils grown at physiologically relevant pH. We provide a structural analysis of three dominant polymorphs, including an atomic model of the main polymorph comprising residues 13–37 in a density map of 4.2-Å resolution.

Results

Polymorphism of IAPP fibrils. For this work, amyloid fibrils were prepared from synthetic human IAPP including the amidated C terminus. Islet amyloid in T2D is typically extracellular, but IAPP aggregation is supposedly initiated intracellularly, possibly in the secretory granules at a pH of 5.0–6.0 (refs. ^{3,29}); therefore, IAPP fibrils were prepared at a pH of 6.0. Long, well-ordered fibrils were obtained, as shown by atomic force microscopy (AFM) imaging (Extended Data Figs. 1 and 2). We could differentiate at least five different polymorphs in the AFM images and in subsequently performed cryo-EM experiments. Of these five polymorphs, three were

¹Institute of Biological Information Processing (IBI-7: Structural Biochemistry), Forschungszentrum Jülich, Jülich, Germany. ²Jülich Centre for Structural Biology (JuStruct), Forschungszentrum Jülich, Jülich, Germany. ³Institut für Physikalische Biologie, Heinrich Heine University Düsseldorf, Düsseldorf, Germany.

⁴The Multimodal Molecular Imaging Institute, Maastricht University, Maastricht, the Netherlands. ⁵Physics Department, Heinrich Heine University Düsseldorf, Düsseldorf, Germany. ⁶These authors contributed equally: Christine Röder, Tatsiana Kupreichyk. [✉]e-mail: wolfgang.hoyer@uni-duesseldorf.de; gu.schroeder@fz-juelich.de

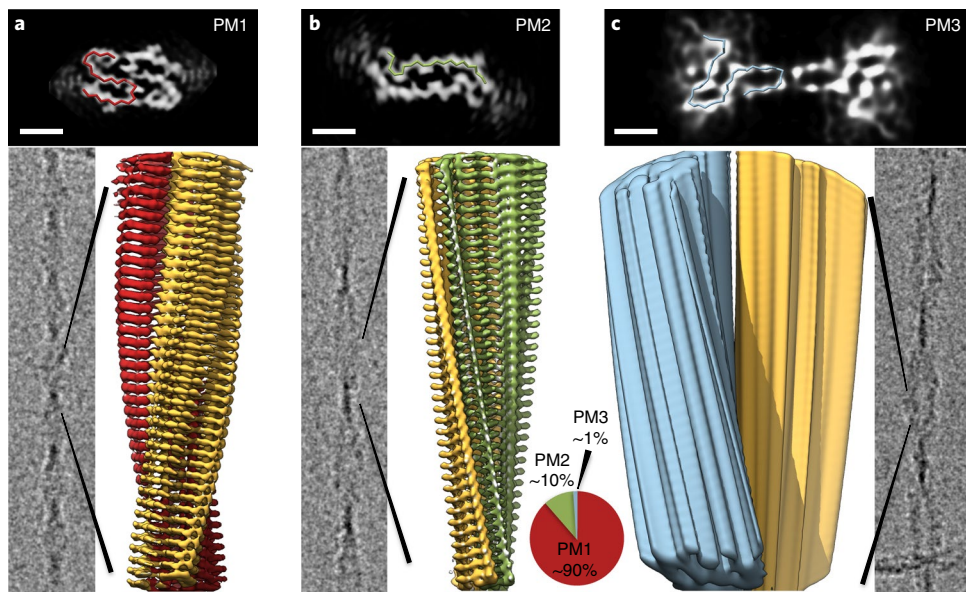


Fig. 1 | Comparison of reconstructed IAPP polymorphs. **a–c**, PM1 (**a**), PM2 (**b**) and PM3 (**c**). For each polymorph, three panels are shown: a slice of a 3D reconstruction superimposed on the respective $\text{C}\alpha$ chain for one monomer (black; scale bars, 2 nm); a micrograph displaying the respective polymorph (gray); and 3D density (red/yellow, PM1 (**a**); green/yellow, PM2 (**b**); blue/yellow, PM3 (**c**)). The pie chart visualizes the fraction of each polymorph in the dataset.

present in sufficient amounts for further analysis (Fig. 1, Table 1, and Extended Data Figs. 1 and 2). The main polymorph, polymorph 1 (PM1), makes up ~90% of all fibrils, while polymorph 2 (PM2) and polymorph 3 (PM3) represent up to ~10% and ~1%, respectively, of the total number of fibrils in the dataset.

PM1 has a right-handed helical symmetry with a pitch of 48 nm and a width of 2.5–4.5 nm (Figs. 1a and 2a). Three-dimensional (3D) reconstruction of 1,161 individual fibril images using a helical pseudo- 2_1 symmetry led to 4.2-Å resolution, which was sufficient to unambiguously build an atomic model with helical parameters of 2.35 Å (helical rise) and 178.23° (helical twist). The fibril consists of two stacks of S-shaped IAPP monomers winding around each other. Further details of the structure and molecular characteristics of PM1 are described later.

PM2 also consists of two protofilaments and exhibits pseudo- 2_1 symmetry (Fig. 1b). With a maximum and minimum width of 52 Å and 17 Å, respectively, PM2 shows a more pronounced twist in the projection images (Fig. 1b) and is remarkably flatter than PM1 (Fig. 1a). The helical pitch is 94 nm, and AFM experiments suggest a left-handed twist. In contrast to the S-shaped PM1, the density map indicates an extended conformation of two IAPP monomers in PM2. The protofilament interface consists of a continuous sequence region of at least 18 amino acids. The density map with approximately 4.2-Å resolution would in principle allow for model building of 21 amino acid residues, but the sequence assignment is ambiguous. Therefore, we modeled all 17 possible sequence assignments in both forward and backward backbone trace directions, leading to $17 \times 2 = 34$ different models. All 34 models were refined in DireX³⁰ using cross-validation in the resolution range of 3.0–4.0 Å for calculation of the C_{free} value³¹. Results were ranked by C_{free} value (Extended Data Fig. 3). According to this criterion, the most probable model for PM2, which also exhibits the highest C_{work} value, shares important features with the PM1 model, as discussed below.

Compared to the other polymorphs, PM3 was not well represented in the micrographs. The overall features of PM3, namely the broad width (110 Å) and pronounced twist (159-nm pitch), lead to a dumbbell shape (Fig. 1c). From the 4,591 particles extracted, we could reconstruct a density with 8.1-Å resolution. Because the

resolution was rather low, we were not able to build an atomic model but only hypothesize a possible $\text{C}\alpha$ backbone trace (Fig. 1c). Nonetheless, the density also clearly indicates two symmetric protofilaments and reveals that the 10-Å-wide protofilament interface of PM3, presumably consisting of three residues, is very small compared to those of PM1 and PM2 (Fig. 1).

Fibril architectures of PM1 and PM2. In PM1, each monomer exhibits an overall S-fold that comprises residues Ala13–Tyr37 (Fig. 2). Up to residue 12, the N-terminal part including the disulfide bond between Cys2 and Cys7 is largely disordered and, therefore, does not reveal clear density (Fig. 1a). The side view of PM1 shows the typical cross-β pattern of amyloid fibril structures with a spacing of 4.7 Å between the layers (Fig. 2c). The cross-β layers are well resolved in the density, as shown in Fig. 2d. On the secondary structure level, we observed three β-sheets: residues 14–20, 26–32 and 35–37. Figure 3b shows the comparison of our model with former secondary structure predictions based on sequence analysis²², NMR^{23,26,27}, electron paramagnetic resonance (EPR)²⁵ and X-ray crystallography experiments²⁴.

The cross-section of the PM1 fibril displays two monomeric S-folds related by approximate 2_1 symmetry (Fig. 2b). The double-S shape is stabilized by both hydrophobic and polar interactions. The central part of the protofilament interface contains a hydrophobic cluster comprising residues Phe23, Gly24, Ala25 and Leu27 as well as Phe23', Gly24', Ala25' and Leu27' (Fig. 2b and Extended Data Fig. 4). Additionally, the backbone of Phe23 and Ala25 forms hydrogen bonds at the center of the fibril, thereby connecting one subunit with two neighboring subunits above and below in the opposing protofilament (Fig. 3c). More precisely, there is a hydrogen bond between the carbonyl group of Phe23 of chain *i* and the amide group of Ala25 of chain *i*+1 and another hydrogen bond between the amide group of Ala25 of chain *i* and the carbonyl group of Phe23 of chain *i*-1. The backbone around Gly24 does not maintain the cross-β hydrogen-bonding pattern along the fibril. The aforementioned interactions are formed by residues located in the sequence motif (N)NFGAIL, shown earlier to be important for fibrillization of IAPP^{5,32–34}. This motif is located in the central part

Table 1 | Cryo-EM data collection, refinement and validation statistics

	PM1 (EMD-10669, PDB 6Y1A)	PM2 (EMD-10670)	PM3 (EMD-10671)
Data collection and processing			
Magnification	110,000	110,000	110,000
Voltage (kV)	200	200	200
Dose rate (e ⁻ Å ⁻² s ⁻¹)	0.9	0.9	0.9
Exposure time (s)	46	46	46
Movie frames (no.)	1,800	1,800	1,800
Defocus range (μm)	−1.0 to −2.2	−1.0 to −2.2	−1.0 to −2.2
Pixel size (Å)	0.935	0.935	0.935
Symmetry imposed	helical, pseudo 2 ₁	helical, pseudo 2 ₁	helical, pseudo 2 ₁
Helical rise (Å)	2.351	2.352	2.323
Helical twist (°)	178.23	179.10	179.47
Helical pitch (Å)	479.5	940	1590
Final fibril images (no.)	1,161	1,480	99
Final particle images (no.)	37,120	24,011	4,591
Map resolution (Å)	4.2	4.2	8.1
FSC threshold	0.143	0.143	0.143
Refinement			
Initial density model used	Noise-filled cylinder	Noise-filled cylinder	Noise-filled cylinder
Model composition			
Non-hydrogen atoms	2,975		
Protein residues	416		
R.m.s. deviations			
Bond lengths (Å)	0.0039		
Bond angles (°)	0.60		
Validation			
MolProbity score	1.99		
Clashscore	15.2		
Poor rotamers (%)	0		
Ramachandran plot			
Favored (%)	95.7		
Allowed (%)	4.3		
Disallowed (%)	0		

of the structure, in the turn between the first two β-sheets (Figs. 2b and 3a,b). Within this turn, the kink around Phe23 and Asn21 is stabilized by hydrogen bonds between Asn22 and Ser19, as well as between Asn22 and Gly24 (Figs. 2b and 3c). Additionally, Ile26 might support this turn by hydrophobic interactions with Val17. In the second turn, between β-sheets 2 and 3, Asn31 together with Ser29, Asn35 and Tyr37 creates a hydrophilic cluster at the C terminus of IAPP with possible interactions between Asn31 and Ser29, as well as Asn31 and Asn35. In addition, Tyr37 might interact with both Asn35 and Ser29 (Fig. 2b). Moreover, the amidated C terminus itself forms a polar ladder (Fig. 3d). This ladder is further connected to Asn21' of the opposite protofilament with slightly longer and, therefore, weaker hydrogen bonds. The overall cross-β arrangement is further stabilized by Asn14, Asn21 and Asn31, which form polar ladders alongside the fibril axis. Asn22 does not form a polar ladder, but instead its N82 atom forms a hydrogen bond with the carbonyl group of Gly24 within the same monomer (Fig. 3c). It should be noted that the detailed analysis of the hydrogen-bonding network is derived from the atomic model, which is an interpretation of the experimental density map.

IAPP contains an unusually large number of the polar residues asparagine, serine and threonine⁵. We found that these residues form polar streaks within the fibril core of PM1 (Extended Data Fig. 4). The polar streaks are characterized by extensive networks of hydrogen bonds, as discussed earlier. The segregation of polar and apolar residues into distinct clusters within the fibril core likely contributes to the high stability of IAPP amyloid. In IAPP, this segregation is facilitated by the preorganization of amino acid residues in polar and apolar clusters within the primary structure, in the fashion of a block copolymer with polar blocks 19-SSNN-22 and 28-SSTN-31 and apolar block 23-FGAIL-27.

All-atom molecular dynamic (MD) simulations were performed to evaluate the overall stability of the model. In two independent 250-ns simulations, the model remained stable (Extended Data Fig. 5) with an all-atom r.m.s. deviation (r.m.s.d.) of a single subunit from the deposited model of ~2 Å and an r.m.s. fluctuation (r.m.s.f.) of residues 16–37 of 0.8 Å. The N-terminal part including Phe15 was already substantially more mobile (Extended Data Fig. 5a,b,e). Notably, we observed ladder formation for Asn22 in the MD simulation, which was not supported by the density map.

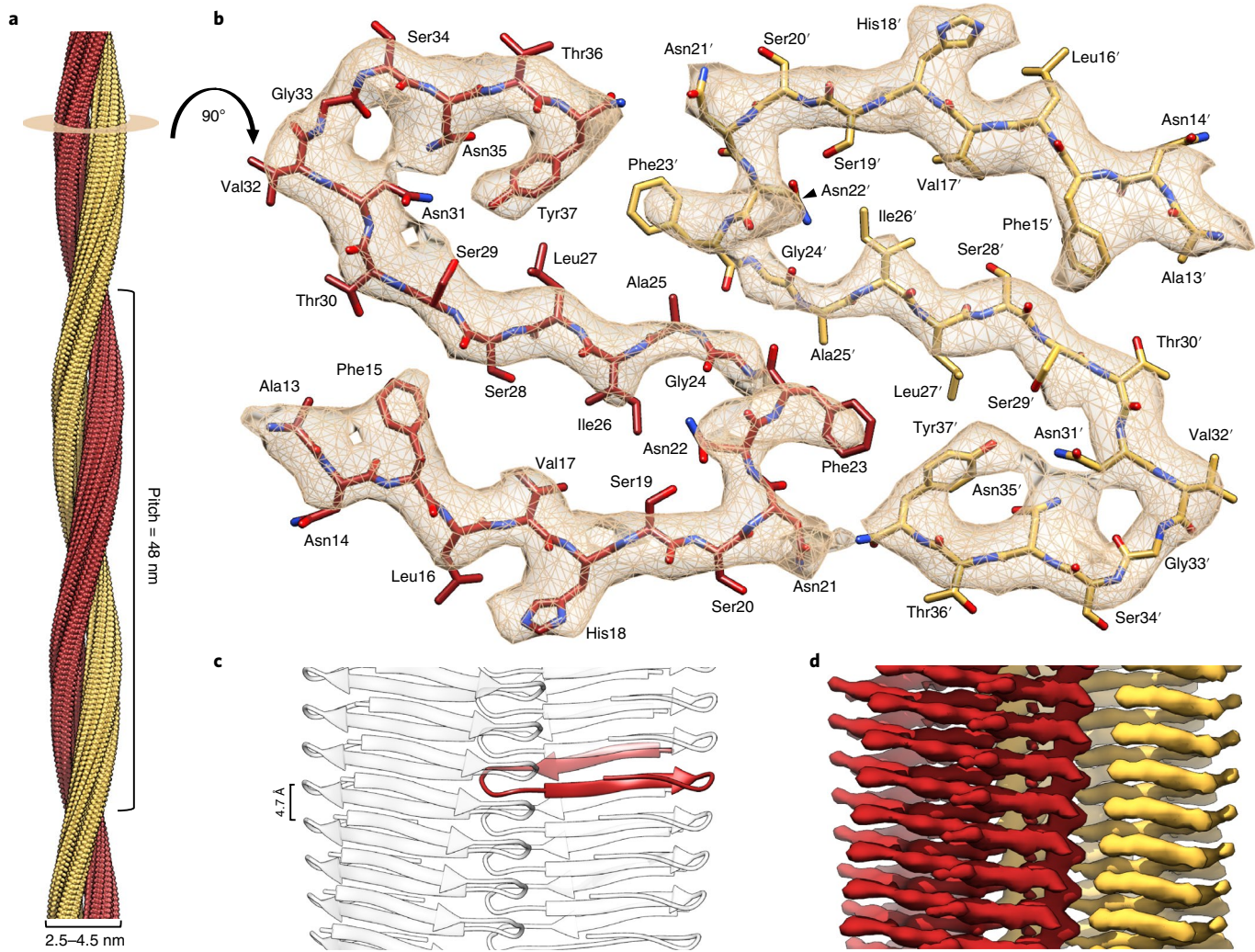


Fig. 2 | Architecture of the main polymorph, PM1. **a**, PM1 exhibits a helical pitch of 48 nm and a minimum and maximum width of 2.5 and 4.5 nm, respectively. The fibril consists of two protofilaments (red and yellow). **b**, Cross-sectional view: two symmetry-related monomers, with an atomic model of residues 13–37 built into the 4.2-Å-resolution density (contour level of 1.5σ). **c**, Side view: one monomer is highlighted (red) to show its integration in the fibrillar structure. Cross-β layers are separated by 4.7 Å. **d**, Side view: reconstructed density corresponding to **c**.

For earlier structures of amyloid fibrils, we discussed the need for a minimal fibril unit, which is the smallest fibril structure fragment in which the capping subunits at both ends would have established the same full contact interface with other constituting monomers as the capping subunits of an extended fibril^{35,36}. Here, the minimal fibril unit consists of only three monomers, which is the smallest possible unit. One subunit is in contact exclusively with its neighboring monomers above and below and with its opposing monomers through protofilament interface contacts (Fig. 2c). Indeed, we did not observe any interlocking of different cross-β layers, which was postulated to have a stabilizing effect on other amyloid fibrils^{35,36}.

The IAPP folds in PM1 and PM2 are clearly distinct, yet the most probable model for PM2 shares important features with the PM1 model (Extended Data Fig. 3). First, the NFGAIL motif forms the center of the fibril interface. Second, the N terminus is rather flexible and thus not resolved in the density map. The first visible residue in the density of the PM2 model is Phe15. In contrast to PM1, not only the N terminus but also the two C-terminal residues Thr36 and Tyr37 are not clearly resolved and are potentially mobile. In between the two protofilaments is a relatively large cavity lined by hydrophobic residues Phe23, Ala25 and Ile26. It is not clear whether this gap is water filled.

Similar S-folds in IAPP and Aβ fibrils. Colocalization of IAPP and Aβ has been observed in patients with T2D and AD¹⁹. The epidemiological link between diabetes and dementia might be explained by cross-seeding of IAPP and Aβ aggregation^{19,20,37,38}. Different sites on amyloid fibrils are relevant for cross-seeding: cross-elongation (that is, the elongation of a fibril with a heterologous protein) occurs at the fibril end, while cross-nucleation (that is, the fibril-catalyzed formation of a heterologous fibril nucleus) may occur both at the fibril end and along the fibril surface. Like IAPP, Aβ forms different fibril polymorphs, according to ssNMR and cryo-EM studies^{35,39–43}. Comparing IAPP PM1 to multiple Aβ_{1–42} polymorphs containing S-shaped folds^{35,40,44}, we found that the backbones superimpose (Fig. 4b,c). The structural similarity of the backbones is highest when superimposing the models in an antiparallel arrangement (Fig. 4c). The similarity between IAPP and Aβ_{1–42} fibril folds regarding topology and size might promote cross-seeding at the fibril end, which could further be supported by the sequence similarity of IAPP and Aβ²¹. The sequence similarity is highest around the Gly-Ala-Ile segment at positions 24–26 of IAPP and positions 29–31 of Aβ. In both IAPP and Aβ, this segment is located in the solvent-excluded center of the S-fold (Fig. 4d). A further segment that can be superimposed in parallel arrangement is the N-terminal strand of the

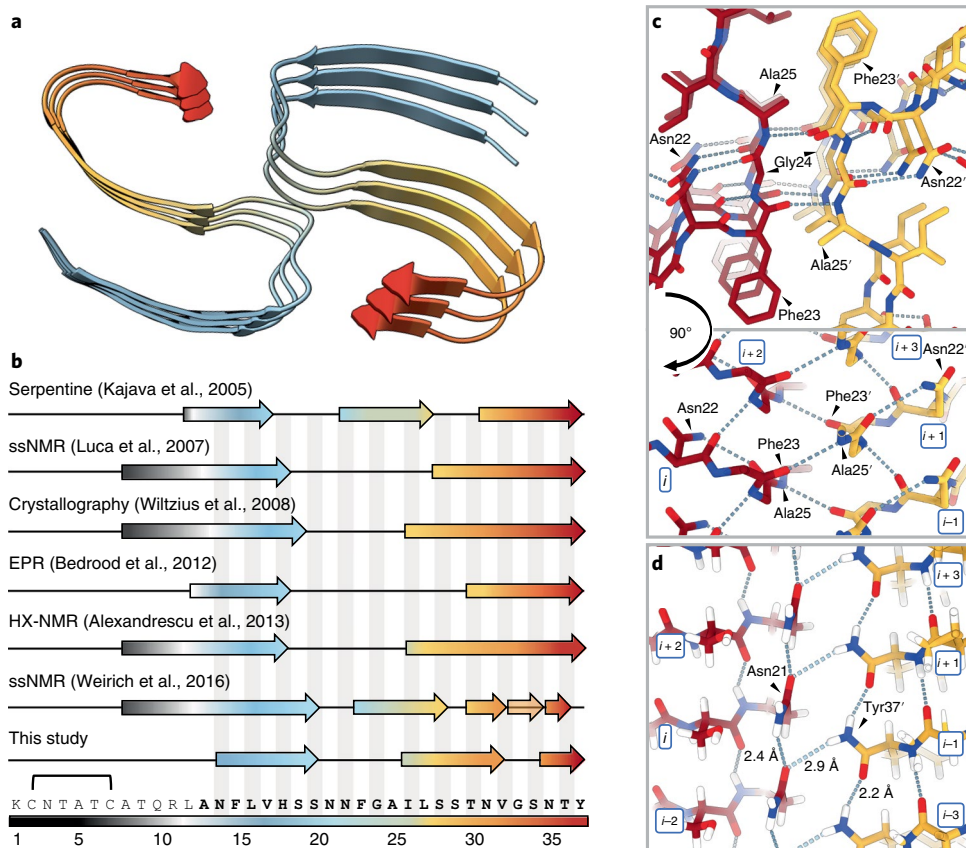


Fig. 3 | Secondary structure and hydrogen bonding in PM1. **a**, Secondary structure of the IAPP model. Tilted cross-section of three fibril layers with representation of the three β -sheets. **b**, Comparison of our PM1 structure to former models derived from sequence-based prediction²², EPR²⁵, ssNMR²⁷, X-ray crystallography²⁴ and hydrogen-exchange NMR (HX-NMR) studies²⁶. Arrows indicate β -sheets (one potential β -sheet is shown as transparent). The disulfide bridge between residues Cys2 and Cys7 is indicated. Fibril formation was performed at pH 7.4 (refs. ^{23,25–27}) or 6.5 (ref. ²⁴), while our IAPP fibrils were formed at pH 6.0. **c**, Top view of the fibril core showing the two NFGAIL motifs in the opposing protofilaments (red and yellow), as well as the hydrogen-bonding network (dashed lines). Bottom, side view of the fibril core illustrating the interlocking of the protofilaments by hydrogen bonds. **d**, Side view of the fibril showing the hydrogen-bonding interaction of Asn21 with the amidated C terminus of the opposing protofilament (yellow), as well as polar ladders of Asn21 and Tyr37' along the fibril axis.

S-fold in IAPP PM1 and in the LS-shaped $\text{A}\beta_{1–42}$ polymorph, corresponding to 14-NFLVHSSNN-22 of IAPP and 16-KLVFAEDV-24 of $\text{A}\beta$ (Fig. 4d).

A serine-to-glycine substitution at position 20 (Ser20Gly), the only known IAPP genetic polymorphism in humans, is associated with early onset of T2D^{45,46}. The Ser20Gly substitution enhances aggregation and toxicity of IAPP and leads to increased beta-cell apoptosis^{47–50}. Substitution of serine with glycine has been suggested to promote turn formation at residue 20, favoring the amyloid fibril conformation^{51,52}. In line with this notion, Ser20 is located at the edge of the turn comprising residues 20–25 in PM1. Interestingly, when comparing the S-fold of IAPP with the LS-fold of $\text{A}\beta$ ³⁵ (Fig. 4c,d), the Ser20Gly substitution in IAPP and the Arctic mutation (encoding a Glu22Gly substitution) of $\text{A}\beta$ ⁵³, which causes early-onset AD, are located at corresponding positions (Fig. 4d). This suggests that these two replacements with glycine might have analogous conformational consequences.

Discussion

The IAPP fibril samples investigated here displayed fibril polymorphism. While all three main polymorphs consist of two (pseudo)symmetric, helically intertwined protofilaments, they exhibit substantial differences in the protein fold (Fig. 1). PM1 consists of a compact S-shaped fold, PM2 features an extended IAPP conformation and the PM3 cross-section shows two compact motifs connected

by an extended bridge. Marked differences are also observed between the protofilament interfaces: in PM1, the interface consists of one of the turns and the C-terminal end of the S-fold; in PM2, the entire extended IAPP segment that constitutes the fibril core is involved in the protofilament interface; and in PM3, a very narrow interface of probably only three residues is observed. Despite these differences, certain IAPP sequence segments might contribute similarly to distinct fibril polymorphs—in both PM1 and the most probable PM2 model, residues 22–NFGAIL–27 form the central fibril core.

In an early report²⁸ of IAPP fibril polymorphism, the most common polymorph consisted of two protofilaments coiled around each other with a helical pitch of 50 nm, while another polymorph showed a helical pitch of 100 nm. These values are in good agreement with PM1 (48 nm) and PM2 (94 nm). Despite these similarities, when comparing the cryo-EM results with previous structural data, it must be considered that variations may arise from differences between both the applied techniques and the polymorphs present in the samples. In line with previous studies^{22–27}, we found that the IAPP N terminus including the disulfide bond between Cys2 and Cys7 is not part of the fibril core, neither in PM1 (Fig. 3b) nor in the most probable model of PM2 (Extended Data Fig. 3). While well-defined density starts from residue 13 in the cryo-EM data, some studies reported the fibril core to begin around residue 8 (Fig. 3b). However, HX-NMR data indicated that residues 8–14

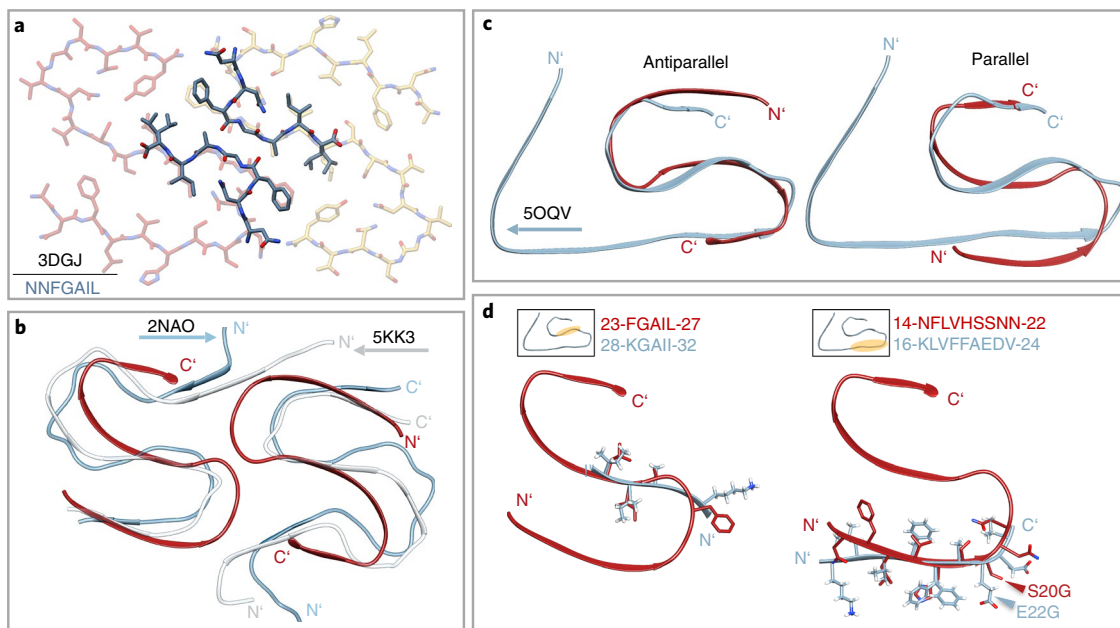


Fig. 4 | Structural comparison of PM1 with fibrillar IAPP peptide and A β fibril models. **a**, Overlay of our model with a crystal structure (dark; 3DGJ) of the NNFGAIL peptide from Wiltzius et al.²⁴. **b**, Overlay of IAPP (red) with NMR structures by Wälti et al.⁴⁰ (light blue; 2NAO) and Colvin et al.⁴⁴ (gray; 5KK3). **c**, Antiparallel (left) and parallel (right) overlay of one IAPP PM1 monomer (red) with the atomic model of A β ₁₋₄₂ (light blue; 5OQV) from Gremer et al.³⁵. **d**, Detailed parallel overlay of sequence segments in IAPP (red) and A β ₁₋₄₂ (light blue; 5OQV) from Gremer et al.³⁵. Small boxes indicate where the respective sequence motif is located in the A β ₁₋₄₂ model. Left, the FGAIL motif of IAPP shows high sequence identity to KGAIL in A β ₁₋₄₂. Right, the NFLVHSSNN motif of IAPP corresponds to the KLVFFAEDV motif of A β (₁₋₄₂) with high structural similarity. Disease-related substitutions in IAPP (Ser20Gly) and A β ₁₋₄₂ (Glu22Gly) are located at corresponding positions.

were less protected than those in the central fibril core²⁶. In agreement with previous data, residues 13–37 are largely in β -sheet conformation in PM1, although variation exists with respect to the precise location of β -strands (Fig. 3b). A common feature of the PM1 cryo-EM structure and previous models is a turn in segment 20-SNNFG-24 (refs. ^{23–27}). A second turn is formed in PM1 in segment 32-VGS-34 and was also supported by ssNMR and HX-NMR studies^{26,27}. Both turns establish an S-shaped fold of IAPP in PM1. Consequently, the tyrosyl ring of the C-terminal Tyr37 packs against Phe23' in the adjacent protofilament, which is in line with distance restraints for IAPP fibrils obtained by fluorescence resonance energy transfer⁵⁴. In addition, these energy-transfer experiments proposed a maximum distance of 11 Å between Tyr37 and a second phenylalanine, coinciding with the Tyr37–Phe15 distance in the PM1 model⁵⁴. The C-terminal amide stabilizes the S-shaped fibril structure by forming a polar ladder and a hydrogen bond with Asn21 in the adjacent protofilament (Fig. 3d), in line with enhanced amyloid formation upon C-terminal amidation of IAPP^{55,56}.

The sequence region at positions 20–29 is particularly important for the amyloidogenicity of IAPP^{5,32,33}. This can be rationalized with the PM1 fibril structure. First, residues 22-NFGAILSS-29 constitute the solvent-excluded central core of PM1 fibrils (Fig. 2b). Second, residues 21-NNFGAIL-27 form, together with Tyr37 and the amidated C terminus, the protofilament interface. In previous structural models of IAPP fibrils, the region encompassing residues 20–29 was associated with formation of a partially ordered loop rather than a β -structure, which was surprising considering the sensitivity of IAPP amyloid formation to mutations mapping to this region⁷. The PM1 fibril structure shows that residues 20–25 indeed form a turn, albeit one that is an integral part of the fibril core, featuring an extensive hydrogen-bonding network (Fig. 3c,d). Residues 26–29, on the other hand, are part of the central β -sheet of IAPP PM1 fibrils. Remarkably, the structure of the 21-NNFGAIL-27 segment in PM1 is highly similar in atomic detail to a crystal structure

of the NNFGAIL peptide²⁴ (Fig. 4a). This applies both to the fold of the individual polypeptide molecules and to the peptide–protofilament interface, which displays extensive main chain–main chain interactions between the 23-FGA-25 segments. The similarity of the NNFGAIL structure between the peptide crystal and the PM1 fibril indicates that the 21-NNFGAIL-27 segment drives IAPP amyloid formation.

In contrast to the human protein, IAPP proteins from several other species were found to be non-amyloidogenic⁵. The non-amyloidogenic rat and mouse IAPP contain six amino acids that are different from the human sequence³³. Five of these are located in the sequence region encompassing residues 23–29, which is part of the central core of PM1 fibrils, as discussed above. The differing amino acids include three prolines in rat and mouse IAPP at positions 25, 28 and 29. As proline disrupts secondary structures, these proline residues are incompatible with the PM1 structure, consistent with the low amyloidogenicity of rat and mouse IAPP. The insights gained from the rat and mouse IAPP sequences were exploited in the design of pramlintide, a non-amyloidogenic IAPP analog carrying proline substitutions at positions 25, 28 and 29 (ref. ⁵⁷). Pramlintide is co-administered with insulin in type 1 diabetes to improve glucose level regulation. Similarly, the combination of a non-amyloidogenic IAPP analog and leptin could be a promising treatment option for obesity⁵⁸. However, these drugs would benefit from increased solubility⁵⁹. The structural data on IAPP fibrils presented here may aid in the design of non-amyloidogenic, soluble IAPP analogs by suggesting potential sites for chemical modifications of IAPP that counteract fibril formation.

This study presents the 4.2-Å-resolution structure of an IAPP fibril polymorph consisting of two S-shaped protofilaments but also highlights the polymorphism of IAPP fibrils. The dominant S-shaped PM1 can rationalize many of the characteristics of IAPP fibrils described by various groups, suggesting that PM1 is a common polymorph or that it at least represents general features of

prevalent IAPP polymorphs. The study provides detailed insight into the link between the IAPP amino acid sequence and fibril structure; furthermore, it reveals similarities between IAPP and A β fibril structures, which are particularly striking in consideration of the link between diabetes and AD. The structural information gained may serve as a basis to define the mechanisms of amyloid formation and toxicity of IAPP. Moreover, the PM1 fibril may be used as a target structure to design imaging probes for IAPP fibrils and inhibitors of IAPP fibril growth.

Online content

Any methods, additional references, Nature Research reporting summaries, source data, extended data, supplementary information, acknowledgements, peer review information; details of author contributions and competing interests; and statements of data and code availability are available at <https://doi.org/10.1038/s41594-020-0442-4>.

Received: 12 February 2020; Accepted: 30 April 2020;

Published online: 15 June 2020

References

- Opie, E. L. On the relation of chronic interstitial pancreatitis to the islands of Langerhans and to diabetes mellitus. *J. Exp. Med.* **5**, 397–428 (1901).
- Jurgens, C. A. et al. β -cell loss and β -cell apoptosis in human type 2 diabetes are related to islet amyloid deposition. *Am. J. Pathol.* **178**, 2632–2640 (2011).
- Westerman, P., Andersson, A. & Westerman, G. T. Islet amyloid polypeptide, islet amyloid, and diabetes mellitus. *Physiol. Rev.* **91**, 795–826 (2011).
- Wimalawansa, S. J. Amylin, calcitonin gene-related peptide, calcitonin, and adrenomedullin: a peptide superfamily. *Crit. Rev. Neurobiol.* **11**, 167–239 (1997).
- Akter, R. et al. Islet amyloid polypeptide: structure, function, and pathophysiology. *J. Diabetes Res.* **2016**, 2798269 (2016).
- Mulkherjee, A., Morales-Scheihing, D., Butler, P. C. & Soto, C. Type 2 diabetes as a protein misfolding disease. *Trends Mol. Med.* **21**, 439–449 (2015).
- Cao, P., Abedini, A. & Raleigh, D. P. Aggregation of islet amyloid polypeptide: from physical chemistry to cell biology. *Curr. Opin. Struct. Biol.* **23**, 82–89 (2013).
- Halban, P. A. et al. β -cell failure in type 2 diabetes: postulated mechanisms and prospects for prevention and treatment. *J. Clin. Endocrinol. Metab.* **99**, 1983–1992 (2014).
- Zraika, S. et al. Toxic oligomers and islet beta cell death: guilty by association or convicted by circumstantial evidence? *Diabetologia* **53**, 1046–1056 (2010).
- Zhang, S. et al. The pathogenic mechanism of diabetes varies with the degree of overexpression and oligomerization of human amylin in the pancreatic islet β cells. *FASEB J.* **28**, 5083–5096 (2014).
- Masters, S. L. et al. Activation of the NLRP3 inflammasome by islet amyloid polypeptide provides a mechanism for enhanced IL-1 β in type 2 diabetes. *Nat. Immunol.* **11**, 897–904 (2010).
- Rivera, J. F. et al. Human IAPP disrupts the autophagy/lysosomal pathway in pancreatic β -cells: protective role of p62-positive cytoplasmic inclusions. *Cell Death Differ.* **18**, 415–426 (2011).
- Gupta, D. & Leahy, J. L. Islet amyloid and type 2 diabetes: overproduction or inadequate clearance and detoxification? *J. Clin. Invest.* **124**, 3292–3294 (2014).
- Casas, S. et al. Impairment of the ubiquitin–proteasome pathway is a downstream endoplasmic reticulum stress response induced by extracellular human islet amyloid polypeptide and contributes to pancreatic β -cell apoptosis. *Diabetes* **56**, 2284–2294 (2007).
- Hull, R. L. et al. Amyloid formation in human IAPP transgenic mouse islets and pancreas, and human pancreas, is not associated with endoplasmic reticulum stress. *Diabetologia* **52**, 1102–1111 (2009).
- Janson, J., Ashley, R. H., Harrison, D., McIntyre, S. & Butler, P. C. The mechanism of islet amyloid polypeptide toxicity is membrane disruption by intermediate-sized toxic amyloid particles. *Diabetes* **48**, 491–498 (1999).
- Paulsson, J. F. et al. High plasma levels of islet amyloid polypeptide in young with new-onset of type 1 diabetes mellitus. *PLoS ONE* **9**, e93053 (2014).
- Martinez-Valbuena, I. et al. Interaction of amyloidogenic proteins in pancreatic β cells from subjects with synucleinopathies. *Acta Neuropathol.* **135**, 877–886 (2018).
- Oskarsson, M. E. et al. In vivo seeding and cross-seeding of localized amyloidosis: a molecular link between type 2 diabetes and Alzheimer's disease. *Am. J. Pathol.* **185**, 834–846 (2015).
- Moreno-Gonzalez, I. et al. Molecular interaction between type 2 diabetes and Alzheimer's disease through cross-seeding of protein misfolding. *Mol. Psychiatry* **9**, 1327–1334 (2017).
- O'Nuallain, B., Williams, A. D., Westerman, P. & Wetzel, R. Seeding specificity in amyloid growth induced by heterologous fibrils. *J. Biol. Chem.* **279**, 17490–17499 (2004).
- Kajava, A. V., Aebi, U. & Steven, A. C. The parallel superpleated β -structure as a model for amyloid fibrils of human amylin. *J. Mol. Biol.* **348**, 247–252 (2005).
- Luca, S., Yau, W. M., Leapman, R. & Tycko, R. Peptide conformation and supramolecular organization in amylin fibrils: constraints from solid-state NMR. *Biochemistry* **46**, 13505–13522 (2007).
- Wiltzius, J. J. W. et al. Atomic structure of the cross- β spine of islet amyloid polypeptide (amylin). *Protein Sci.* **17**, 1467–1474 (2008).
- Bedrood, S. et al. Fibril structure of human islet amyloid polypeptide. *J. Biol. Chem.* **287**, 5235–5241 (2012).
- Alexandrescu, A. T. Amide proton solvent protection in amylin fibrils probed by quenched hydrogen-exchange NMR. *PLoS ONE* **8**, e56467 (2013).
- Weirich, F. et al. Structural characterization of fibrils from recombinant human islet amyloid polypeptide by solid-state NMR: the central FGAILS segment is part of the β -sheet core. *PLoS ONE* **11**, e0161243 (2016).
- Goldsbury, C. S. et al. Polymorphic fibrillar assembly of human amylin. *J. Struct. Biol.* **119**, 17–27 (1997).
- Hutton, J. C. The internal pH and membrane potential of the insulin-secretory granule. *Biochem. J.* **204**, 171–178 (1982).
- Wang, Z. & Schröder, G. F. Real-space refinement with DireX: from global fitting to side-chain improvements. *Biopolymers* **97**, 687–697 (2012).
- Falkner, B. & Schröder, G. F. Cross-validation in cryo-EM-based structural modeling. *Proc. Natl. Acad. Sci. USA* **110**, 8930–8935 (2013).
- Westerman, P., Engstrom, U., Johnson, K. H., Westerman, G. T. & Betsholtz, C. Islet amyloid polypeptide: pinpointing amino acid residues linked to amyloid fibril formation. *Proc. Natl. Acad. Sci. USA* **87**, 5036–5040 (1990).
- Betsholtz, C. et al. Sequence divergence in a specific region of islet amyloid polypeptide (IAPP) explains differences in islet amyloid formation between species. *FEBS Lett.* **251**, 261–264 (1989).
- Tenidis, K. et al. Identification of a penta- and hexapeptide of islet amyloid polypeptide (IAPP) with amyloidogenic and cytotoxic properties. *J. Mol. Biol.* **295**, 1055–1071 (2000).
- Gremer, L. et al. Fibril structure of amyloid- β (1–42) by cryo-electron microscopy. *Science* **358**, 116–119 (2017).
- Röder, C. et al. Atomic structure of PI3-kinase SH3 amyloid fibrils by cryo-electron microscopy. *Nat. Commun.* **10**, 3754 (2019).
- Janson, J. et al. Increased risk of type 2 diabetes in Alzheimer's disease. *Diabetes* **53**, 474–481 (2004).
- Yang, Y. & Song, W. Molecular links between Alzheimer's disease and diabetes mellitus. *Neuroscience* **250**, 140–150 (2013).
- Colvin, M. T. et al. Atomic resolution structure of monomeric A β ₄₂ amyloid fibrils. *J. Am. Chem. Soc.* **138**, 9663–9674 (2016).
- Wälti, M. A. et al. Atomic-resolution structure of a disease-relevant A β _{1–42} amyloid fibril. *Proc. Natl. Acad. Sci. USA* **113**, 4976–4984 (2016).
- Xiao, Y. et al. A β _{1–42} fibril structure illuminates self-recognition and replication of amyloid in Alzheimer's disease. *Nat. Struct. Mol. Biol.* **22**, 499–505 (2015).
- Kollmer, M. et al. Cryo-EM structure and polymorphism of A β amyloid fibrils purified from Alzheimer's brain tissue. *Nat. Commun.* **10**, 4760 (2019).
- Colvin, M. T. et al. Atomic resolution structure of monomeric A β ₄₂ amyloid fibrils. *J. Am. Chem. Soc.* **138**, 9663–9674 (2016).
- Sakagashira, S. et al. Missense mutation of amylin gene (S20G) in Japanese NIDDM patients. *Diabetes* **45**, 1279–1281 (1996).
- Seino, S. S20G mutation of the amylin gene is associated with type II diabetes in Japanese. Study Group of Comprehensive Analysis of Genetic Factors in Diabetes Mellitus. *Diabetologia* **44**, 906–909 (2001).
- Meier, D. T. et al. The S20G substitution in hIAPP is more amyloidogenic and cytotoxic than wild-type hIAPP in mouse islets. *Diabetologia* **59**, 2166–2171 (2016).
- Cao, P. et al. Sensitivity of amyloid formation by human islet amyloid polypeptide to mutations at residue 20. *J. Mol. Biol.* **421**, 282–295 (2012).
- Sakagashira, S. et al. S20G mutant amylin exhibits increased in vitro amyloidogenicity and increased intracellular cytotoxicity compared to wild-type amylin. *Am. J. Pathol.* **157**, 2101–2109 (2000).
- Ma, Z. et al. Enhanced in vitro production of amyloid-like fibrils from mutant (S20G) islet amyloid polypeptide. *Amyloid* **8**, 242–249 (2001).
- Xu, W., Jiang, P. & Mu, Y. Conformation preorganization: effects of S20G mutation on the structure of human islet amyloid polypeptide segment. *J. Phys. Chem. B* **113**, 7308–7314 (2009).
- Mirecka, E. A. et al. β -hairpin of islet amyloid polypeptide bound to an aggregation inhibitor. *Sci. Rep.* **6**, 33474 (2016).
- Nilsberth, C. et al. The 'Arctic' APP mutation (E693G) causes Alzheimer's disease by enhanced A β protofibril formation. *Nat. Neurosci.* **4**, 887–893 (2001).

54. Padrick, S. B. & Miranker, A. D. Islet amyloid polypeptide: identification of long-range contacts and local order on the fibrillogenesis pathway. *J. Mol. Biol.* **308**, 783–794 (2001).
55. Chen, M. S. et al. Characterizing the assembly behaviors of human amylin: a perspective derived from C-terminal variants. *Chem. Commun.* **49**, 1799–1801 (2013).
56. Yonemoto, I. T., Kroon, G. J. A., Dyson, H. J., Balch, W. E. & Kelly, J. W. Amylin proprotein processing generates progressively more amyloidogenic peptides that initially sample the helical state. *Biochemistry* **47**, 9900–9910 (2008).
57. Kruger, D. F. & Gloster, M. A. Pramlintide for the treatment of insulin-requiring diabetes mellitus: rationale and review of clinical data. *Drugs* **64**, 1419–1432 (2004).
58. Roth, J. D. et al. Leptin responsiveness restored by amylin agonism in diet-induced obesity: evidence from nonclinical and clinical studies. *Proc. Natl Acad. Sci. USA* **105**, 7257–7262 (2008).
59. Wang, H., Abedini, A., Ruzsicska, B. & Raleigh, D. P. Rationally designed, nontoxic, nonamyloidogenic analogues of human islet amyloid polypeptide with improved solubility. *Biochemistry* **53**, 5876–5884 (2014).

Publisher's note Springer Nature remains neutral with regard to jurisdictional claims in published maps and institutional affiliations.

© The Author(s), under exclusive licence to Springer Nature America, Inc. 2020

Methods

Sample preparation. Human IAPP (H-KCNTATCATQLANFLVHSSNNFGA ILSSSTNVGSNTY-NH₂; molecular mass 3903.4 Da) with an amidated C terminus and a disulfide bond between Cys2 and Cys7 was custom synthesized (Pepscan, Lelystad). Identity and purity (93.1%) were confirmed by reverse-phase HPLC (RP-HPLC) and mass spectroscopy. RP-HPLC of a reduced sample confirmed that the disulfide bond between Cys2 and Cys7 was fully established in the non-reduced sample. To ensure monomeric starting material, the peptide was dissolved at 2 mg ml⁻¹ in 1,1,1,3,3,3-hexafluoro-2-propanol at room temperature for 1 h and lyophilized. Afterward, 1 mg peptide powder was dissolved in 0.5 ml aqueous 6 M guanidine hydrochloride solution, and size-exclusion chromatography was performed on a Superdex 75 Increase 10/300 column (GE Healthcare) equilibrated with 10 mM 2-(N-morpholino)ethanesulfonic acid (MES)/NaOH buffer at a pH of 6.0 using an ÄKTA Purifier system (GE Healthcare). The monomeric peak fraction was collected, aliquotted, flash frozen in liquid nitrogen and stored at -80°C for further use. The purity of the IAPP monomer fraction was 93.8% according to RP-HPLC. IAPP fibrils were prepared from the stock solution by diluting to a final concentration of 100 μM peptide with 10 mM MES/NaOH buffer (pH 6.0, 6 mM NaN₃). Fibrillation occurred by incubation within 7 d at room temperature under quiescent conditions in 1.5-ml Protein LoBind tubes (Eppendorf). As a control, we also prepared fibrils from an IAPP monomer sample of increased purity (96.9% after size-exclusion chromatography) due to an additional preparative RP-HPLC purification step preceding monomerization. All three dominant polymorphs were recovered in this sample, indicating that increasing peptide purity does not affect aggregation kinetics or thermodynamics in a way that would result in monomorphic fibrillation.

Atomic force microscopy. IAPP fibrils in 10 mM MES/NaOH buffer (pH 6.0, 6 mM NaN₃) were diluted to a peptide concentration of 10 μM monomer equivalent. Afterward, 5 μl of the fibril solution was applied to freshly cleaved muscovite mica and incubated under a humid atmosphere for 10 min. After three washing steps with 100 μl ddH₂O, the samples were dried with a stream of N₂ gas. Imaging was performed in intermittent contact mode (AC mode) in a Nano Wizard 3 atomic force microscope (JPK, Berlin) using a silicon cantilever and tip (OMCL-AC160TS-R3, Olympus) with a typical tip radius of 9 ± 2 nm, a force constant of 26 N m⁻¹ and a resonance frequency of approximately 300 kHz. The images were processed using JPK data processing software (version spm-5.0.84). For the height profiles presented, a polynomial fit was subtracted from each scan line, first independently and then using limited data range.

Cryo-electron microscopy image acquisition. Cryo-EM sample preparation was performed on glow-discharged holey carbon films (Quantifoil R 1.2/1.3, 300 mesh). A 2.5-μl sample containing 100 μM IAPP in 10 mM MES/NaOH buffer (pH 6.0, 6 mM NaN₃) was applied to the carbon grid and incubated for 1 min. Subsequently, the sample was blotted for 5 s (blotting force 5) before cryo-plunging using a Vitrobot (FEI). With 110,000-fold nominal magnification, 1,330 micrographs were recorded on a Tecnai Arctica electron microscope operating at 200 kV with a field emission gun using a Falcon III (FEI) direct electron detector in electron counting mode directed by EPU data collection software (version 1.5). Each movie was composed of 50 fractions, and each fraction contained 36 frames, resulting in a total of 1,800 frames recorded per micrograph. The sample was exposed to an integrated flux of 0.9 e⁻ Åring⁻² s⁻¹ for 46.33 s. Applied defocus values ranged from -1 to -2.2 μm. The pixel size was calibrated to 0.935 Å as described previously³⁶. Details of data acquisition are summarized in Table 1.

Cryo-electron microscopy image processing and helical reconstruction. For all polymorphs, MotionCor2 (ref. ⁶⁰) was used for movie correction, and contrast transfer function parameters were fitted with CTFFIND4 (ref. ⁶¹). Fibrils were manually picked, and segments were extracted with an inter-box distance of 10% of the box sizes. Box sizes were chosen as 220 Å, 200 Å and 220 Å for PM1, PM2 and PM3, respectively. Further image processing, including 3D reconstructions, was performed with RELION 3.0.5 (refs. ^{62,63}).

For all polymorphs (PM1, PM2 and PM3), we used a noise-filled cylinder as an initial density model. Initial rounds of density refinement used the relion_refine command without the auto_refine option ($K=1$) and a T value of 20. Final refinements were conducted with a T value of 200. Gold-standard refinements were performed as described previously³⁵ by selecting entire fibrils and splitting the dataset accordingly into an even and an odd set. Fourier shell correlation curves were computed between two half maps. According to the 0.143 criterion, the obtained resolutions were 4.2 Å (PM1), 4.2 Å (PM2) and 8.1 Å (PM3) (Extended Data Figs. 6–8). Image processing and reconstruction details for all polymorphs are presented in Table 1.

Model building and refinement of PM1. For PM1, a single-chain atomic model was built with Coot^{64,65} by placing a polyalanine model de novo into the density. The density was clearly resolved and unambiguously defined the backbone trace. After manual optimization of the protein backbone, side chains were added and rotamers were manually refined with respect to Ramachandran outliers and potential clashes. Five copies of the final single-chain model were placed into the

EM density map. The final model, containing six symmetry-related monomers of IAPP PM1, was used for real-space refinement in PHENIX⁶⁶ with manually assigned β-sheets. Subsequently, the model was refined by multiple rounds of optimization in Coot, PHENIX and MDFF^{67,68}. MDFF was performed using an explicit solvent. The structure was embedded in a box of water, and ions were added to the system (concentration, 1.5 M). Secondary structure, *cis*-peptide and chirality restraints were applied. The scaling factor of the map potential was set to $g=0.3$, and a time period of 10 ns was simulated. The final model of PM1 was obtained by averaging the coordinates of the MDFF trajectory and a final energy minimization with the non-crystallographic symmetry restraints and position restraints using CNS^{69,70}, including hydrogen atoms. B factors were assigned based on r.m.s.f. values calculated from the MDFF trajectory. After model evaluation using MolProbity⁷¹, molecular graphics and further analyses were performed using Chimera⁷² and ChimeraX⁷³. The final statistics of the refinement are shown in Table 1.

Model building and refinement of PM2. Because of the difficulties in assigning residues to the density of PM2, two polyalanine backbones, each containing 21 residues, were built in both forward and backward trace directions in Coot^{64,65}. A total of 17 possible assignments of segments from the IAPP sequence to the 21 residues were visible in the density. Accordingly, we performed 17 side chain assignments for each backbone using Scwrll4 (ref. ⁷⁴). The resulting 34 models were energy minimized with CNS⁶⁹ and refined into the density map using DireX⁷⁰. The C_{free} value³¹ is the real-space map correlation coefficient computed from the density map filtered with a bandpass of 3.0- to 4.0-Å resolution and served as a criterion to rank the models (Extended Data Fig. 3). The model that scored best according to this ranking was further refined using MDFF^{67,68} with the same settings as those for PM1. Refinement was finalized by averaging the coordinates of the MDFF trajectory.

Molecular dynamics simulation. MD simulations were performed to test the stability of the PM1 model. The starting structure for the simulation was built using CHARMM-GUI solution builder^{75,76} by inserting the cryo-EM structure of PM1 into a cubic water box containing 38,907 water molecules and further adding 10 chloride ions to neutralize the system. We carried out two independent all-atom simulations using GROMACS⁷⁷ (version 2019.3) and CHARMM36 force fields for protein⁷⁸, water⁷⁹ and ions⁸⁰. The systems were first minimized using the steepest descent algorithm in 5,000 steps to remove bad contacts, followed by 500 ps (time step, 1 fs) of equilibration in an ensemble with constant volume and temperature. Later, two production runs of 250 ns were conducted under conditions of constant pressure and temperature, with a time step of 2 fs, by applying LINCS constraints to the bonds containing hydrogen atoms⁸¹. The temperature of the systems was maintained at 300 K using a Nosé-Hoover thermostat^{82,83}, and the pressure was maintained at 1 bar with a Parrinello-Rahman barostat⁸⁴. Short-range electrostatic and van der Waals interactions were computed up to a cutoff of 12 Å using potential-shift and force-switch methods, respectively. Long-range electrostatic interactions beyond the 12 Å cutoff were computed using the particle-mesh Ewald algorithm⁸⁵.

Reporting Summary. Further information on research design is available in the Nature Research Reporting Summary linked to this article.

Data availability

The structure of IAPP PM1 has been deposited in the Protein Data Bank under accession code PDB 6Y1A. The cryo-EM density maps have been deposited in the Electron Microscopy Data Bank under accession codes EMD-10669 (PM1), EMD-10670 (PM2) and EMD-10671 (PM3).

References

60. Zheng, S. Q., Palovcak, E., Armache, J.-P., Cheng, Y. & Agard, D. A. MotionCor2: anisotropic correction of beam-induced motion for improved cryo-electron microscopy. *Nat. Methods* **14**, 331–332 (2017).
61. Rohou, A. & Grigorieff, N. CTFFIND4: fast and accurate defocus estimation from electron micrographs. *J. Struct. Biol.* **192**, 216–221 (2015).
62. He, S. & Scheres, S. H. W. Helical reconstruction in RELION. *J. Struct. Biol.* **198**, 163–176 (2017).
63. Scheres, S. H. W. RELION: implementation of a Bayesian approach to cryo-EM structure determination. *J. Struct. Biol.* **180**, 519–530 (2012).
64. Emsley, P. & Cowtan, K. Coot: model-building tools for molecular graphics. *Acta Crystallogr. D Biol. Crystallogr.* **60**, 2126–2132 (2004).
65. Emsley, P., Lohkamp, B., Scott, W. G. & Cowtan, K. Features and development of Coot. *Acta Crystallogr. D Biol. Crystallogr.* **66**, 486–501 (2010).
66. Adams, P. D. et al. PHENIX: a comprehensive Python-based system for macromolecular structure solution. *Acta Crystallogr. D Biol. Crystallogr.* **66**, 213–221 (2010).
67. Trabuco, L. G., Villa, E., Schreiner, E., Harrison, C. B. & Schulzen, K. Molecular dynamics flexible fitting: a practical guide to combine cryo-electron microscopy and X-ray crystallography. *Methods* **49**, 174–180 (2009).

68. Trabuco, L. G., Villa, E., Mitra, K., Frank, J. & Schulten, K. Flexible fitting of atomic structures into electron microscopy maps using molecular dynamics. *Structure* **16**, 673–683 (2008).
69. Brunger, A. T. et al. Crystallography & NMR system: a new software suite for macromolecular structure determination. *Acta Crystallogr. D Biol. Crystallogr.* **54**, 905–921 (1998).
70. Brunger, A. T. Version 1.2 of the Crystallography and NMR system. *Nat. Protoc.* **2**, 2728–2733 (2007).
71. Chen, V. B. et al. MolProbity: all-atom structure validation for macromolecular crystallography. *Acta Crystallogr. D Biol. Crystallogr.* **66**, 12–21 (2010).
72. Petersen, E. F. et al. UCSF Chimera—a visualization system for exploratory research and analysis. *J. Comput. Chem.* **25**, 1605–1612 (2004).
73. Goddard, T. D. et al. UCSF ChimeraX: meeting modern challenges in visualization and analysis. *Protein Sci.* **27**, 14–25 (2018).
74. Krivov, G. G., Shapovalov, M. V. & Dunbrack, R. L. Improved prediction of protein side-chain conformations with SCWRL4. *Proteins* **77**, 778–795 (2009).
75. Jo, S., Kim, T., Iyer, V. G. & Im, W. CHARMM-GUI: a web-based graphical user interface for CHARMM. *J. Comput. Chem.* **29**, 1859–1865 (2008).
76. Lee, J. et al. CHARMM-GUI input generator for NAMD, GROMACS, AMBER, OpenMM, and CHARMM/OpenMM simulations using the CHARMM36 Additive Force Field. *J. Chem. Theory Comput.* **12**, 405–413 (2016).
77. Abraham, M. J. et al. GROMACS: high performance molecular simulations through multi-level parallelism from laptops to supercomputers. *SoftwareX* **1–2**, 19–25 (2015).
78. Best, R. B. et al. Optimization of the additive CHARMM all-atom protein force field targeting improved sampling of the backbone φ , ψ and side-chain χ_1 and χ_2 dihedral angles. *J. Chem. Theory Comput.* **8**, 3237–3256 (2012).
79. MacKerell, A. D. et al. All-atom empirical potential for molecular modeling and dynamics studies of proteins. *J. Phys. Chem. B* **102**, 3586–3616 (1998).
80. Beglov, D. & Roux, B. Finite representation of an infinite bulk system: solvent boundary potential for computer simulations. *J. Chem. Phys.* **100**, 9050–9063 (1994).
81. Hess, B., Bekker, H., Berendsen, H. J. C. & Fraaije, J. G. E. M. LINCS: a linear constraint solver for molecular simulations. *J. Comput. Chem.* **18**, 1463–1472 (1997).
82. Nosé, S. A unified formulation of the constant temperature molecular dynamics methods. *J. Chem. Phys.* **81**, 511–519 (1984).
83. Hoover, W. G. Canonical dynamics: equilibrium phase-space distributions. *Phys. Rev. A Gen. Phys.* **31**, 1695–1697 (1985).
84. Parrinello, M. & Rahman, A. Polymorphic transitions in single crystals: a new molecular dynamics method. *J. Appl. Phys.* **52**, 7182–7190 (1981).
85. Darden, T., York, D. & Pedersen, L. Particle mesh Ewald: an $N\log(N)$ method for Ewald sums in large systems. *J. Chem. Phys.* **98**, 10089–10092 (1993).

Acknowledgements

We thank P.J. Peters and C. López-Iglesias for advice and helpful discussions, H. Duimel for help with sample preparation and the M4I Division of Nanoscopy of Maastricht University for microscope access and support. The authors gratefully acknowledge the computing time granted by the Jülich Aachen Research Alliance High-Performance Computing (JARA-HPC) Vergabegremium and VSR commission on the supercomputer JURECA at Forschungszentrum Jülich. We acknowledge support from a European Research Council (ERC) Consolidator grant (no. 726368; W.H.), the Alzheimer Forschung Initiative e.V. and Alzheimer Nederland (project no. 19082CB; R.B.G.R. and G.F.S.), the Russian Science Foundation (RSF; project no. 20-64-46027; L.G. and D.W.) and the Helmholtz Association Initiative and Networking Fund (project no. ZT-I-0003; K.R.P. and G.F.S.).

Author contributions

L.G., W.H., T.K. and G.F.S. conceived the study. T.K. and L.G. performed and analyzed fibril preparation and AFM experiments. R.G.B.R. performed cryo-EM experiments and the initial data analysis. C.R., T.K. and G.F.S. performed image processing and initial reconstruction. C.R. and G.F.S. performed reconstruction, model building and refinement. L.U.S., K.R.P. and G.F.S. performed molecular dynamics simulations and structure fitting. C.R., T.K., G.F.S., W.H., L.G., K.R.P. and L.U.S. wrote the manuscript. D.W. and all other authors discussed the results and commented on the manuscript.

Competing interests

The authors declare no competing interests.

Additional information

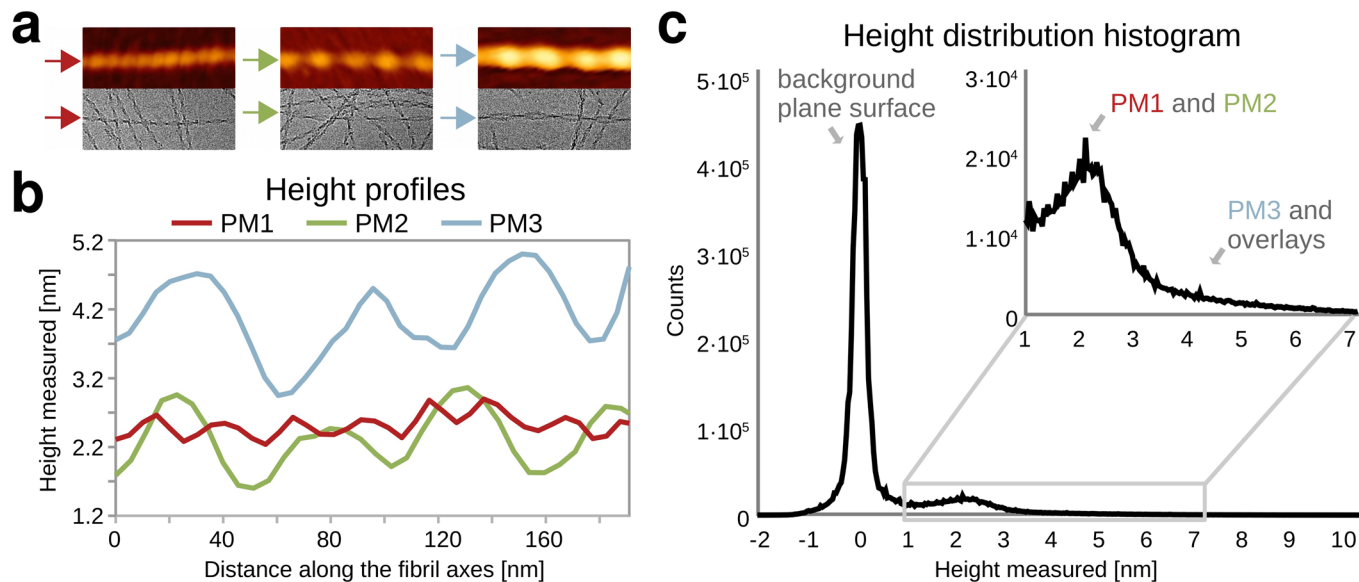
Extended data is available for this paper at <https://doi.org/10.1038/s41594-020-0442-4>.

Supplementary information is available for this paper at <https://doi.org/10.1038/s41594-020-0442-4>.

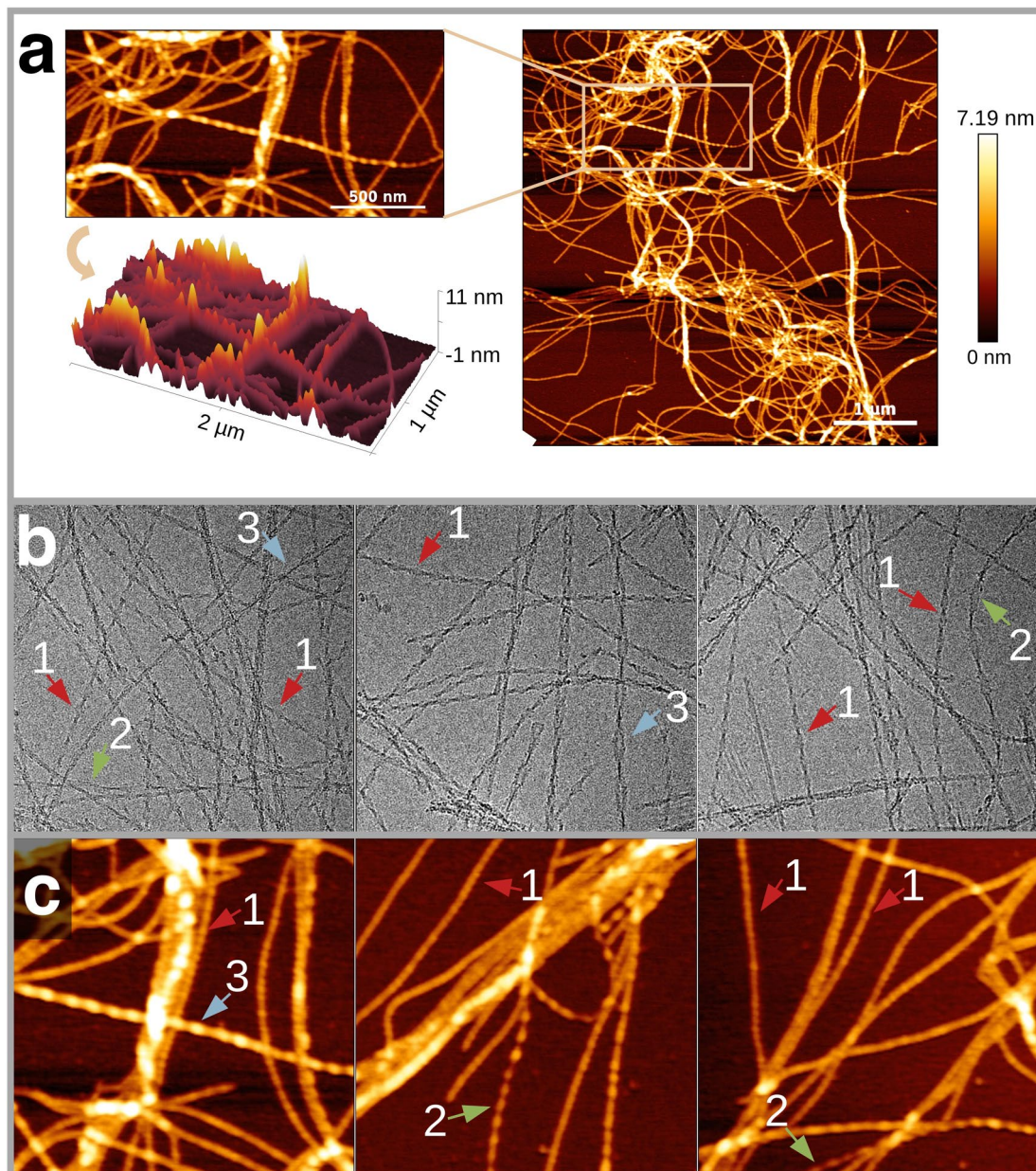
Correspondence and requests for materials should be addressed to W.H. or G.F.S.

Peer review information Peer reviewer reports are available. Inès Chen was the primary editor on this article and managed its editorial process and peer review in collaboration with the rest of the editorial team.

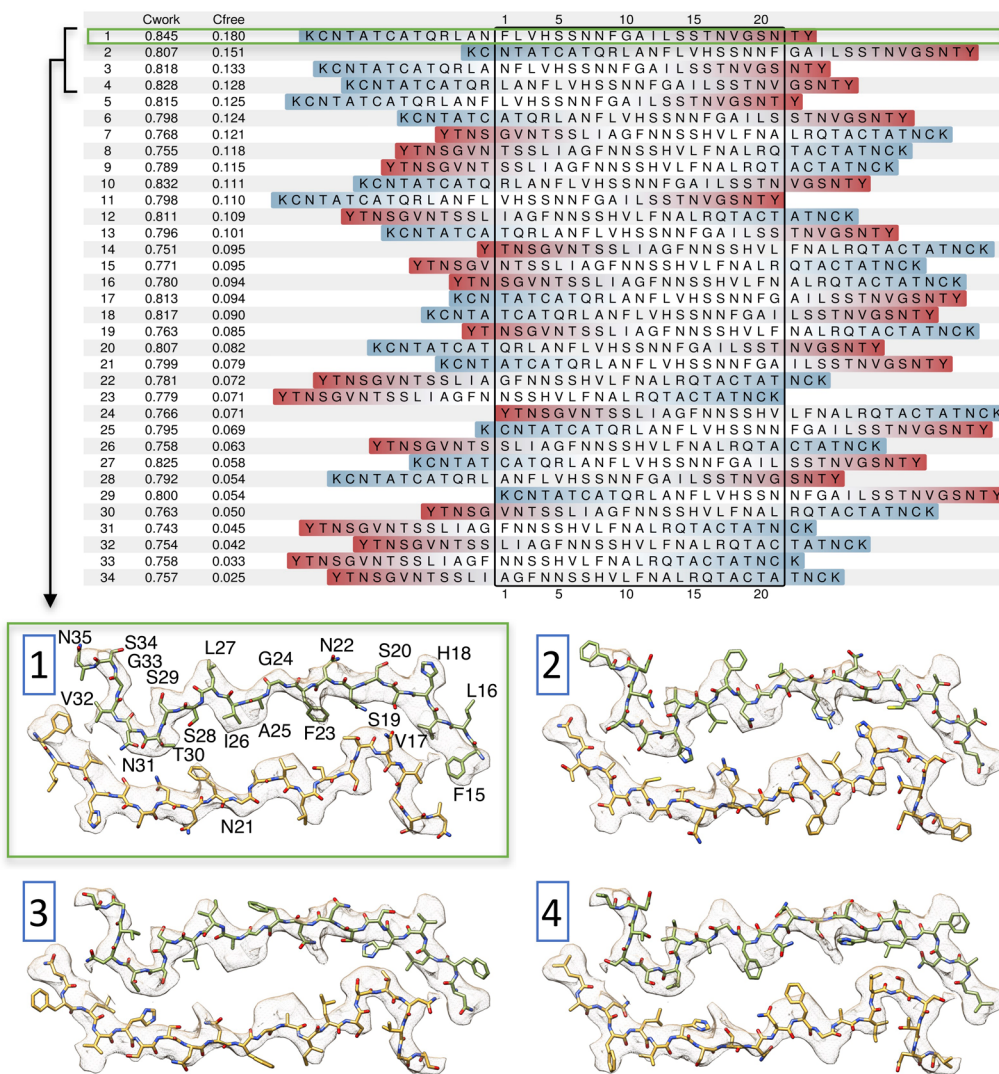
Reprints and permissions information is available at www.nature.com/reprints.



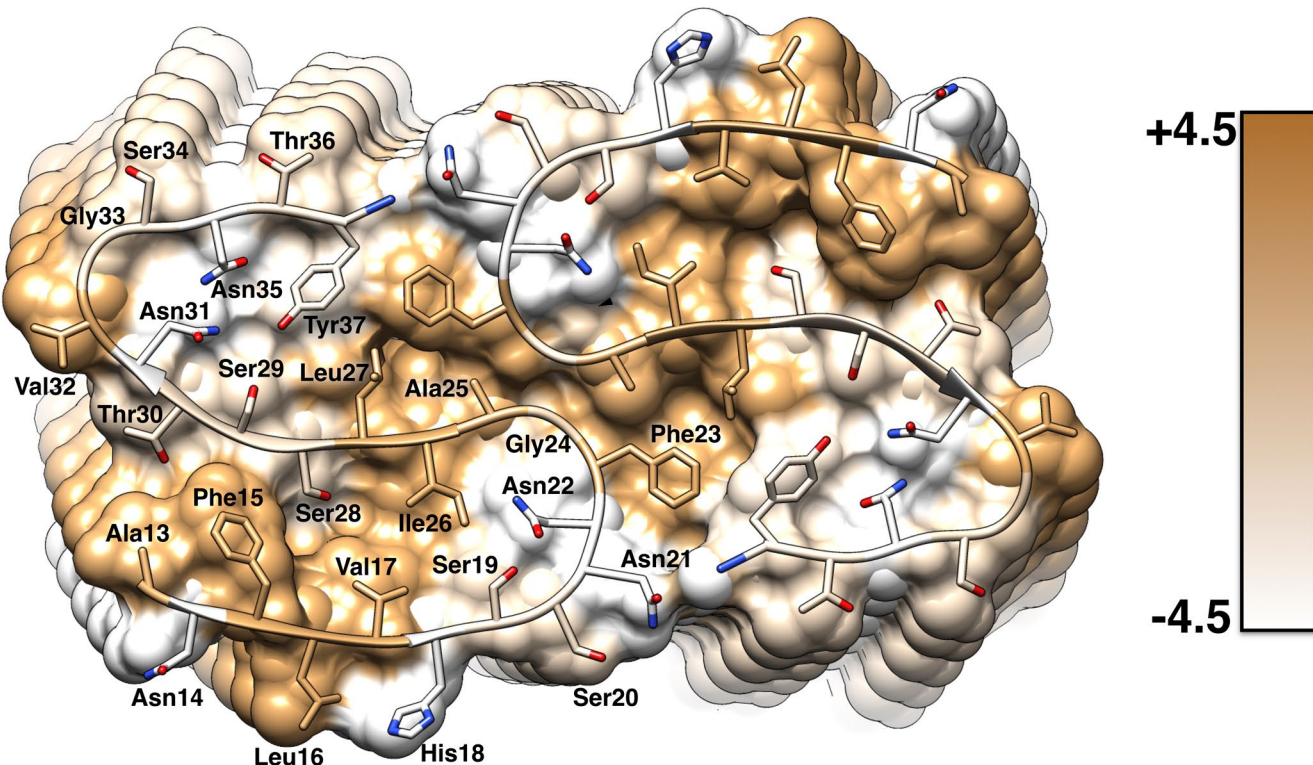
Extended Data Fig. 1 | Comparison of described IAPP polymorphs. **a**, Single fibril cut-outs of polymorphs PM1, PM2 and PM3 from AFM images (top row) and cryo-EM micrographs (bottom row); single box size is 100×250 nm. **b**, Height profiles of individual fibrils extracted from AFM images. **c**, Height distribution histogram, showing the highest number of counts for the plane background surface around 0 nm and a distinct peak around 2.2 nm. The peak around 2.2 nm includes both PM1 and PM2 which are non-distinguishable in sense of height distribution. Moreover, a pronounced shoulder on the right corresponds to the presence of lower amounts of PM3 as well as the overlaps of single PM1/PM2 fibrils. For the height distribution analysis, histograms from six height images of $5 \times 5\text{ }\mu\text{m}$ size and a resolution of 1024×1024 pixels were obtained, binned and presented in one graph. An example of the image used can be seen in Supplementary Figure 2.



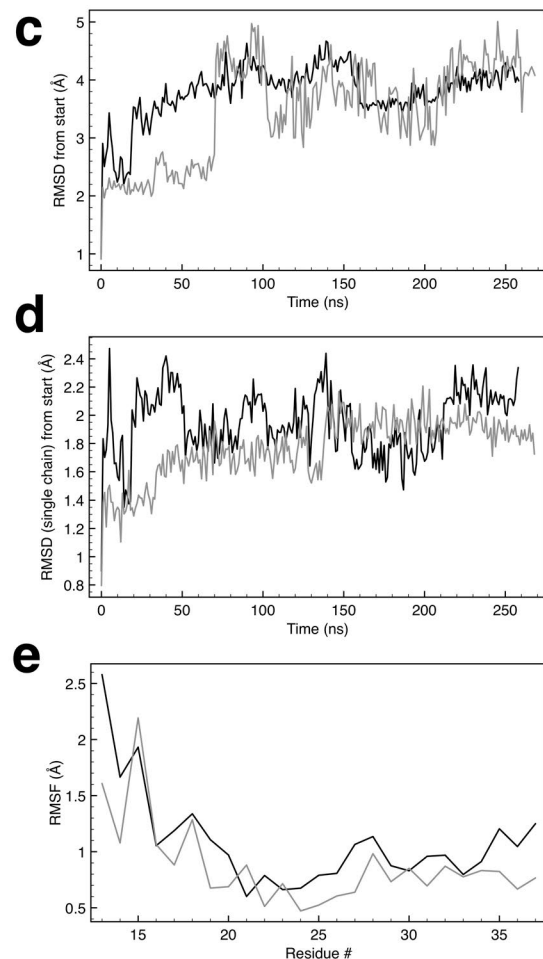
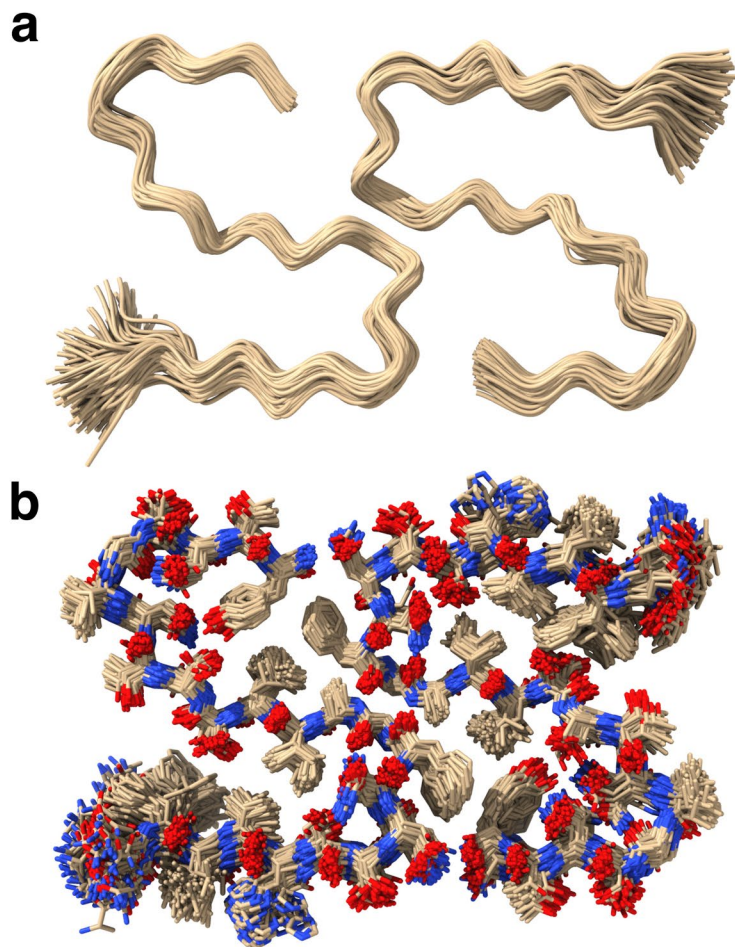
Extended Data Fig. 2 | Overview of IAPP polymorphs. **a**, Typical height profile AFM image used for polymorph distribution analysis. **b**, Cryo-EM micrographs showing 370×370 nm areas. **c**, AFM overview images showing $1 \times 1\text{ }\mu\text{m}$ areas. Arrows indicate the presence of PM1 (red), PM2 (green) and PM3 (blue).



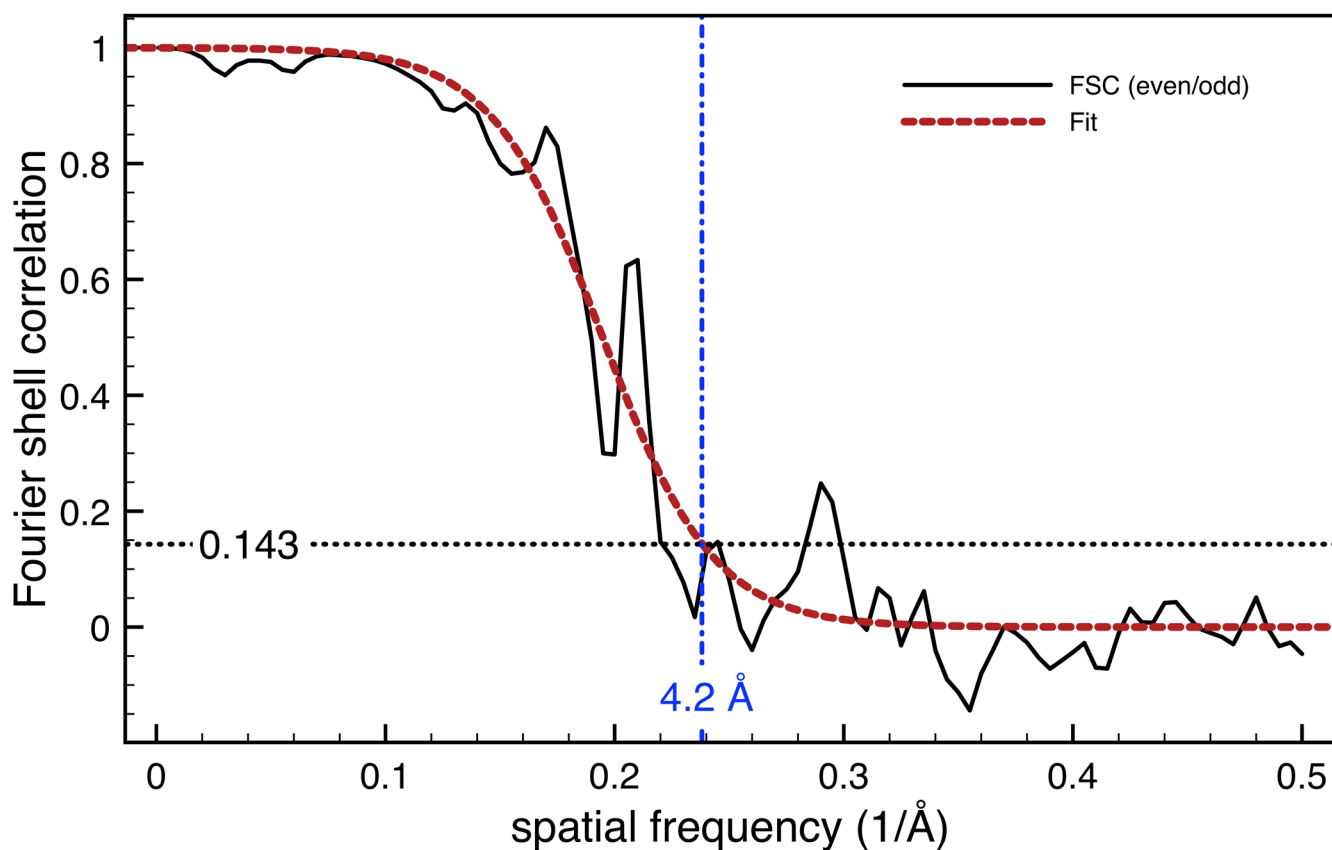
Extended Data Fig. 3 | DireX analysis of polymorph 2 (PM2). The table contains the C_{work} and C_{free} values from DireX fitting of 21-residue-long sequence snippets (black box) of IAPP in both possible C_α-chain directions into a density layer of PM2 together with the respective amino acid sequence. The results are ranked according to their C_{free} values. Highlighted (green box) is the most favorable sequence fit. Atomic models of the four most favorable sequence snippets are shown at the bottom. Note that some models, for example model 2, can be excluded since they are incompatible with the disulfide bond between residues Cys2 and Cys7.



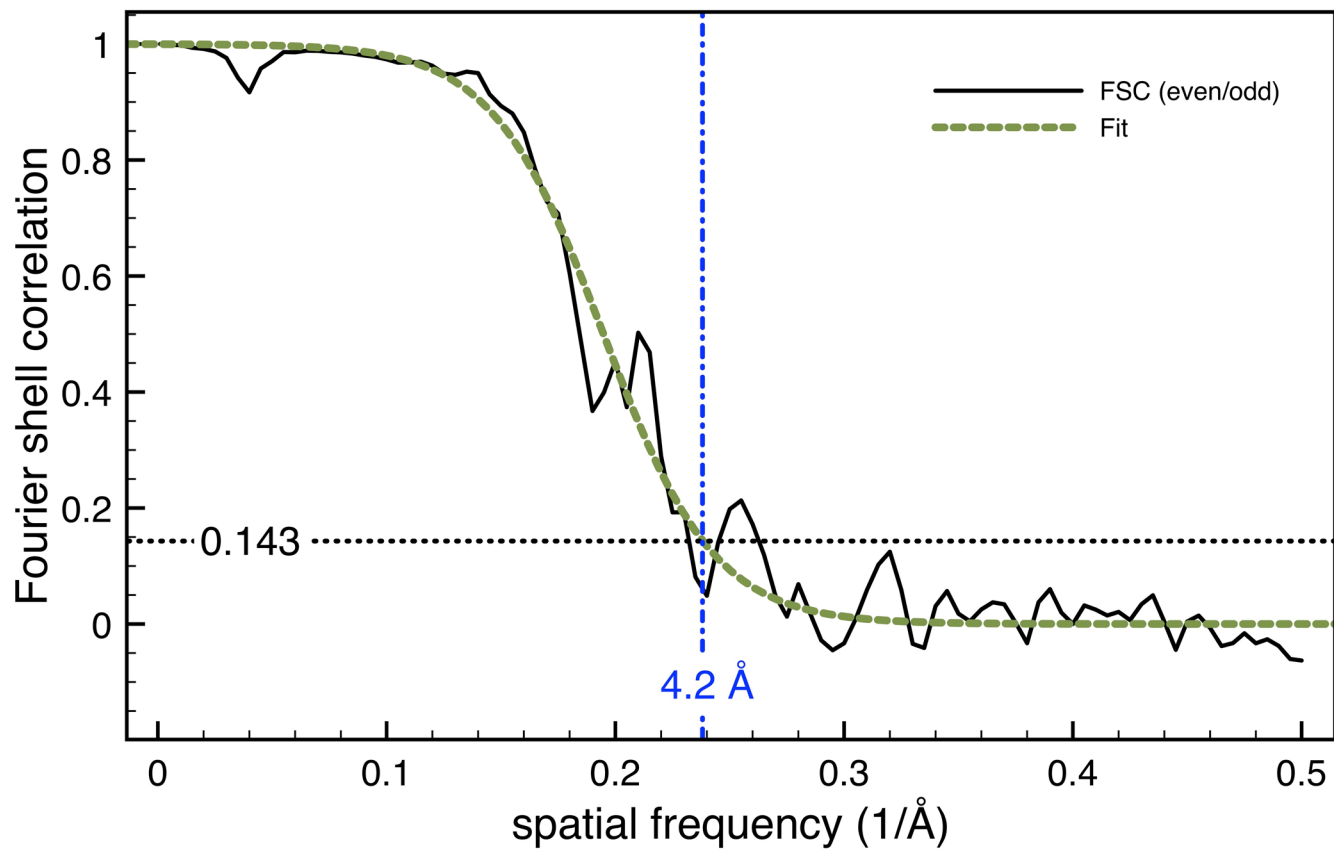
Extended Data Fig. 4 | Hydrophobicity plot of the fibril displayed as top view. Hydrophobicity levels of the IAPP polymorph 1 (PM1) fibril are colored according to Kyte-Doolittle in the hydrophobicity score range –4.5 (white) to 4.5 (gold). One hydrophobic cluster spans the entire diagonal of the fibril cross-section. This hydrophobic streak is surrounded by highly ordered polar clusters.



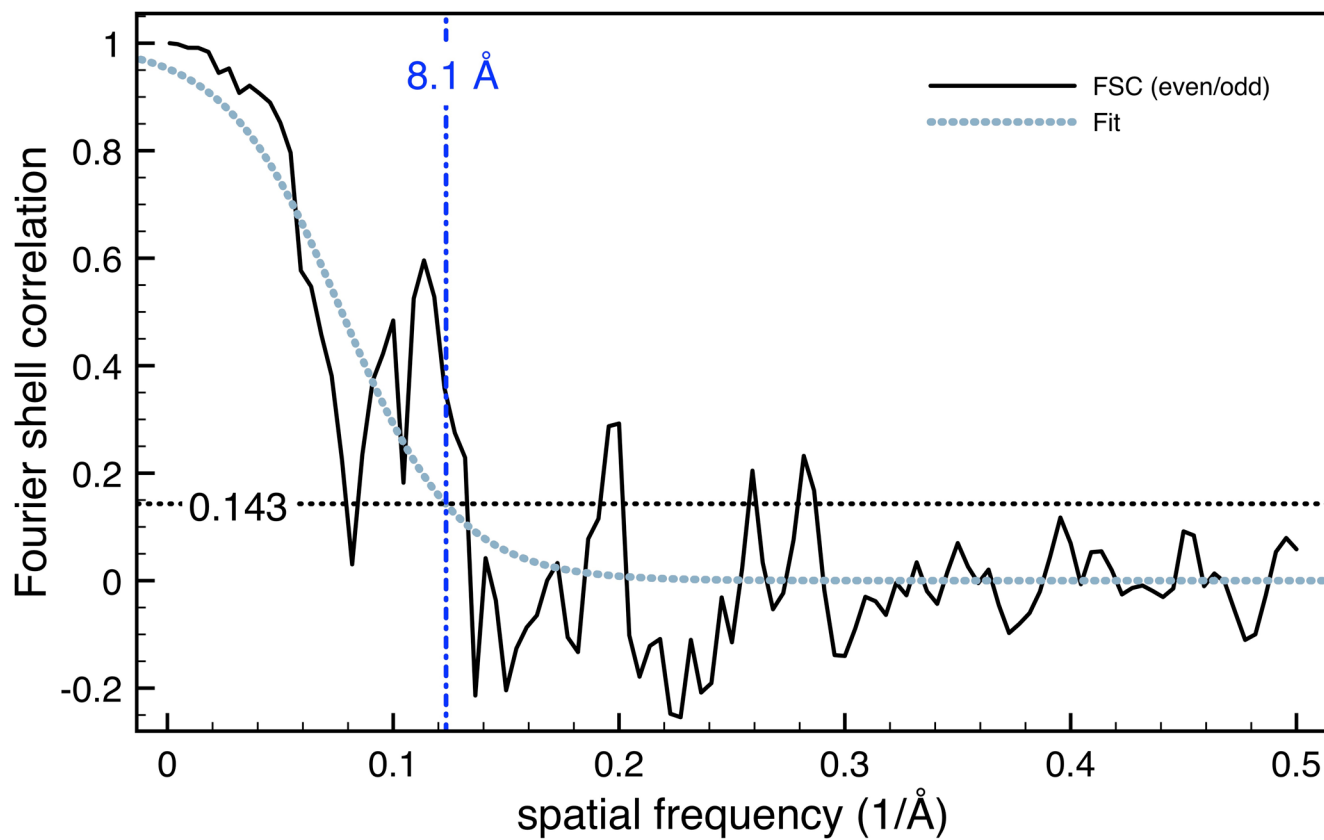
Extended Data Fig. 5 | Results of molecular dynamics simulations of IAPP polymorph 1 (PM1). Superimposed snapshots from a 250 ns simulation displaying only the backbone (a) or all atoms (except for solvent and hydrogen) (b). c, Showing the RMSD from the deposited structure of PM1 (PDB ID 6Y1A) for two 250 ns simulations (black and grey lines, respectively). d, Showing the RMSD of a single chain from the deposited structure during the two 250 ns simulations. e, Showing the atomic root mean square fluctuations (RMSF) for each residue calculated over each 250 ns simulation.



Extended Data Fig. 6 | FSC Analysis of polymorph 1 (PM1). FSC curves from the even/odd test (solid black) from the gold-standard refinement yields a resolution of 4.2 Å (using the 0.143 criterion). The even/odd FSC curve is fitted (red) with the model function $1/(1+\exp((x-A)/B))$ (with $A=0.1947$ and $B=0.026$) to obtain a more robust resolution estimate.



Extended Data Fig. 7 | FSC analysis of polymorph 2 (PM2). FSC curves from the even/odd test (solid black) from the gold-standard refinement yields a resolution of 4.2 Å (using the 0.143 criterion). The even/odd FSC curve is fitted (green) with the model function $1/(1+\exp((x-A)/B))$ (with $A = 0.194789$ and $B = 0.02427$) to obtain a more robust resolution estimate.



Extended Data Fig. 8 | FSC analysis of Polymorph 3 (PM3). FSC curves from the even/odd test (solid black) from the gold-standard refinement yields a resolution of 8.1 Å (using the 0.143 criterion). The even/odd FSC curve is fitted (light blue) with the model function $1/(1+\exp((x-A)/B))$ (with $A = 0.0772$ and $B = 0.0256$) to obtain a more robust resolution estimate.

Reporting Summary

Nature Research wishes to improve the reproducibility of the work that we publish. This form provides structure for consistency and transparency in reporting. For further information on Nature Research policies, see [Authors & Referees](#) and the [Editorial Policy Checklist](#).

Statistics

For all statistical analyses, confirm that the following items are present in the figure legend, table legend, main text, or Methods section.

n/a Confirmed

- The exact sample size (n) for each experimental group/condition, given as a discrete number and unit of measurement
- A statement on whether measurements were taken from distinct samples or whether the same sample was measured repeatedly
- The statistical test(s) used AND whether they are one- or two-sided
Only common tests should be described solely by name; describe more complex techniques in the Methods section.
- A description of all covariates tested
- A description of any assumptions or corrections, such as tests of normality and adjustment for multiple comparisons
- A full description of the statistical parameters including central tendency (e.g. means) or other basic estimates (e.g. regression coefficient) AND variation (e.g. standard deviation) or associated estimates of uncertainty (e.g. confidence intervals)
- For null hypothesis testing, the test statistic (e.g. F , t , r) with confidence intervals, effect sizes, degrees of freedom and P value noted
Give P values as exact values whenever suitable.
- For Bayesian analysis, information on the choice of priors and Markov chain Monte Carlo settings
- For hierarchical and complex designs, identification of the appropriate level for tests and full reporting of outcomes
- Estimates of effect sizes (e.g. Cohen's d , Pearson's r), indicating how they were calculated

Our web collection on [statistics for biologists](#) contains articles on many of the points above.

Software and code

Policy information about [availability of computer code](#)

Data collection

EPU 1.3;

Data analysis

CTFFIND4; MotionCor2; RELION 3.0.5; Phenix 1.11; Coot 0.8.9.1; DireX 0.7.1; Chimera 1.13;

For manuscripts utilizing custom algorithms or software that are central to the research but not yet described in published literature, software must be made available to editors/reviewers. We strongly encourage code deposition in a community repository (e.g. GitHub). See the Nature Research [guidelines for submitting code & software](#) for further information.

Data

Policy information about [availability of data](#)

All manuscripts must include a [data availability statement](#). This statement should provide the following information, where applicable:

- Accession codes, unique identifiers, or web links for publicly available datasets
- A list of figures that have associated raw data
- A description of any restrictions on data availability

Atomic model of PM is available at the PDB ID 6Y1A; EM density maps for polymorphs PM1,PM2, and PM3 are available at EMDB under accession codes EMD-10669, EMD-10670, EMD-10671, respectively.

Field-specific reporting

Please select the one below that is the best fit for your research. If you are not sure, read the appropriate sections before making your selection.

- Life sciences Behavioural & social sciences Ecological, evolutionary & environmental sciences

Life sciences study design

All studies must disclose on these points even when the disclosure is negative.

Sample size	See Supplementary Tables 2 and 3 for number of fibrils and number of fibril segments that were used in structure determination. All cryo-EM fibril images used for structure determination were obtained from one single fibril sample. To confirm that polymorphs were reproducible in terms of structure (helical pitch, diameter) and distribution, we performed electron microscopy and atomic force microscopy on independent IAPP fibril samples.
Data exclusions	No data were excluded.
Replication	All attempts to confirm the reproducibility fibril polymorph structure (helical pitch, diameter) and distribution were successful.
Randomization	not relevant.
Blinding	not relevant.

Reporting for specific materials, systems and methods

We require information from authors about some types of materials, experimental systems and methods used in many studies. Here, indicate whether each material, system or method listed is relevant to your study. If you are not sure if a list item applies to your research, read the appropriate section before selecting a response.

Materials & experimental systems

n/a	Involved in the study
<input checked="" type="checkbox"/>	Antibodies
<input checked="" type="checkbox"/>	Eukaryotic cell lines
<input checked="" type="checkbox"/>	Palaeontology
<input checked="" type="checkbox"/>	Animals and other organisms
<input checked="" type="checkbox"/>	Human research participants
<input checked="" type="checkbox"/>	Clinical data

Methods

n/a	Involved in the study
<input checked="" type="checkbox"/>	ChIP-seq
<input checked="" type="checkbox"/>	Flow cytometry
<input checked="" type="checkbox"/>	MRI-based neuroimaging